AIMS Energy, 14(2): 418–448.
DOI: 10.3934/energy.2026018
Received: 19 August 2025
Revised: 28 January 2026
Accepted: 26 March 2026
Published: 17 April2026

https://www.aimspress.com/journal/energy

Research article

An NSGA-II-based parameter tuning algorithm for EKF-based sliding mode controller of PEM fuel cells

Alireza Beigi and Krishna Vijayaraghavan*

School of Mechatronic Systems Engineering, Simon Fraser University, 250-13450 102 Avenue, Surrey, B.C. V3T 0A3, Canada

* **Correspondence:** Email: krishna@sfu.ca; Tel: +17788500320.

Abstract: This paper addresses the challenge of tracking an arbitrary power profile in a proton exchange membrane fuel cell (PEMFC) in the presence of measurement noise and disturbances. To this end, we used an extended Kalman filter (EKF) to estimate the internal states of the PEMFC in conjunction with an adaptive sliding mode controller (SMC) that has been shown to reduce chatter. The model used by the controller captures the internal dynamics and nonlinearly, and is accurate within 0.1% of the high-fidelity model. We developed the conditions necessary for the stability of the proposed controller based on the Lyapunov stability theorem. We also developed a systematic multi-objective optimization methodology of the controller hyperparameters to simultaneously minimizing tracking error, controller-chatter, and controller input using the non-dominated sorting genetic algorithm II (NSGA-II). The controller performance was demonstrated using multiple simulated experiments. Based on experimental results on desired signal data, we concluded that the proposed controller scheme can track desired power profiles within a 1% error.

Keywords: sliding mode control; optimization; fuel cell; power profile tracking; observer; chattering

Symbols

Symbol	Description	Value used	Unit
γ_*	Mode coefficient		-
ϕ_0, ϕ_1	Mode of concentration		atm
$\phi_{H2,A}^{in}$	Anode inlet hydrogen conc.	1.485	atm
$\phi_{O2,C}^{in}$	Inlet input oxygen conc.	0.21	atm
$\phi_{O2,eff}$	Effective oxygen conc.	-	atm
ρ_0	Constant used in R_{ohm}	6×10^{-3}	ohm
ρ_J	Constant used in R_{ohm}	4×10^{-5}	ohm/A
ρ_T	Constant used in R_{ohm}	5×10^{-5}	ohm/K
τ_0	The time constant of mode 0	6	s
τ_1	The time constant of mode 1	0.67	s
τ_{act}	Activation driving const.		s
τ_{actH2}	Equivalent driven time const.		s
ζ	Weight fraction for channel oxygen concentration	0.5	
χ_*^*	Molar concentration		-
Γ_{ch}	Oxygen flux in the channel		mol/s
$\mathbb{f}$	Vector function of states		-
$\mathbb{g}_*$	Vector function multiplying inputs and noise		-
h	Function defining output		-
v	Measurement noise	$\sim(0,0.01)$	V
w_J	Process (input) noise	$\sim(0,4)$	A/m^2
w_{V0}	Process (input) noise	$\sim(0,0.002)$	V
x_*	System states		-
y, P	The output voltage		-
z	Number of electrons transferred		-
A_{fc}	Area of the fuel cell	0.05	m^2
B_{conc}	Proportionality constant for E_{cell}	0.05	V
C_C	Boost converter capacitor	0.025	F
C_{DL}	Double layer capacitance		F
D	Diffusion coefficient		m^2/s
E_{cell}	Open-circuit voltage		V
$E_{0,cell}$	Standard voltage	1.2271	V
F	Faraday constant	96485	C/mol
$\mathcal{F}$	Vector function of states for the derivative		-
$\mathcal{H}$	Vector function defining output		-
J	Input average current		A/m^2
J_0, J_1	Mode of current density		A/m^2
J_{act}	Activation current density		A/m^2
J_{H2-O}	Hydrogen exchange current density		A/m^2
J_{O2-0}	Exchange current density		A/m^2
L	Effective diffusion length		m
L_C	Boost converter inductance	0.01	H
$\dot{N}_A$	Total anode molar flow rate	7.036×10^{-4}	mol/s

Continued on next page

Symbol	Description	Value used	Unit
$\dot{N}_c$	Total cathode molar flow rate	7.036×10^{-4}	mol/s
$\dot{N}_{O2,C}^{in}$	Total cathode inlet oxygen molar flow rate		mol/s
P_{atm}	Atmospheric pressure		atm
Q_w	Covariance of w in EKF	$diag\ (0.004,0.004)$	
R	Universal gas constant	8.314	J/K/mol
R_L	Boost converter resistance	4	ohm
R_{ohm}	Ohmic resistance		ohm
R_v	Covariance of v in EKF	10	
T_{fc}	Fuel cell temperature	341.5	K
V_O	Output voltage of the boost converter		V
V_{act}	Activation voltage loss		V
$V_{act,0}$	Activation voltage constant		V
V_{cell}	Cell output voltage loss		V
V_{ohm}	Ohmic voltage loss		V
$V_{act,H2-O}$	Activation voltage constant in the driven mode		V

1. Introduction

The proton exchange membrane fuel cell (PEMFC) offers high efficiency and high power density, while operating at low temperatures and having zero emissions [1–3]. This makes PEMFCs one of the more promising technologies to replace fossil fuels, particularly in automotive applications [1–3]. However, the use of PEMFCs in automotive applications would require them to efficiently track the constantly changing power requirements.

Fuel cells are highly nonlinear systems with strongly coupled dynamics. Numerous studies have developed advanced control strategies to control voltage [4,5], temperature [6,7], current [8], and air-feed systems [9,10]. Li and Yu [5] employed distributed deep reinforcement learning and proposed an algorithm to control the output voltage of fuel cells. Haung et al. [7] proposed a control schema to regulate the temperature of the fuel cell stack to combat temperature variation-induced degradation. Several dynamical PEMFC models have been proposed for different geometric configurations to model reaction kinetics and reactant transport [11,12]. Biert et al. [13] proposed 1D dynamic modeling of a solid oxide fuel cell (SOFC) to analyze it in both single-cell and stack formation. Su et al. [14] developed 3D dynamic modeling of a single-cell SOFC in a multi-physics coupled configuration by utilizing a focused ion beam-scanning electron microscopy approach. Ghorbani and Vijayaraghavan [15] designed a simplified quasi-2D method to model a single cell of a planar SOFC, while Javaid et al. [16,17] provided an overview of a nonlinear model and observer-based control of fuel cells. Ebrahimi et al. [18] focused on examining the phenomenon of cathode hydrogen pumping capacity when the cathode is starved and studied the transient model of a starved fuel cell capturing both voltage and hydrogen emission. Romey et al. [19] proposed an extended Kalman filter (EKF) model based on this pseudo-2D model of the PEMFC to estimate oxygen concentration in the cathode.

Fuel cell systems typically consist of multiple fuel cells connected in series and a power converter, in addition to other auxiliary sub-systems. The power converter helps to efficiently match the voltage of the fuel cell stack voltage to the load voltage and can be controlled to extract maximum power. Despite considerable advances in controlling PEMFCs, efficient power tracking remains challenging owing to the nonlinearity of the power curve and multi-time scale response of fuel cell systems [20,21].

Bahri et al. [22] proposed a golden section search (GSS)-based maximum power point tracking (MPPT) controller for a PEMFC power system using a DC/DC boost converter. Kiran et al. [23] utilized a cuckoo search-based fuzzy controller to control the boost converter to increase the voltage and power of the fuel cell stack. Percin et al. [24] proposed a whale optimization algorithm-based MPPT controller for the PEMFC integrated with a boost converter. Zhong et al. [25] developed a two-loop cascade controller with a DC/DC converter to provide the highest possible power of the integrated system in operation. Lorenz et al. [26] proposed a method and an apparatus to control the power of an electric vehicle that is powered by a fuel cell. This patent proposes controlling the energy to match the vehicle demand without specifying technical details. In another patent, Mufford et al. [27] proposed a method to control the power of vehicles, including a fuel cell power system and fuel cell oxidant supply. Lauzze et al. [28] proposed a feedback controller for a simplistic PEMFC model to solve the power set-point tracking problem. Kolavennu et al. [29] designed a power profile tracking method that is stabilized using Lyapunov theory to control the automobile powered by a fuel cell. However, existing power tracking control approaches do not consider DC/DC converter impact and noise.

Sliding-mode controllers (SMCs) are one of the most popular controllers for tracking problems owing to their inherent robustness to external disturbance and uncertainties, and their fast response [30–36]. SMCs work in two phases—first the controller applies a large discontinuous control input to drive the system states to a specific "sliding surface" within the state-space domain; once the system reaches this surface, the inherent stability of the surface or a feedback control drives the system state trajectory to the desired state trajectory [30]. Many research works were conducted to investigate the performance of SMCs for solving the trajectory tracking problem in different control applications such as marine vessels [30], autonomous underwater vehicles [31], spherical robots [32], quadrotors [33], and fuel cell systems [9,34–36]. Silaa et al. [37] proposed an SMC to track the load current by ignoring the fuel cell dynamics and noise, while Xu et al. [38] proposed an SMC to track the load voltage by considering a simplified model of the fuel cell and ignoring noise.

Owing to the discontinuous nature of SMCs, they suffer from a phenomenon known as chattering, where the control input continuously oscillates between two values. One of the effective methods to alleviate the chattering in a linearized system is known as describing-function tuning [39–42]. However, this approach is useful for systems that can be linearized about a certain point or can be represented as a set of linear systems [41]. Other approaches involve an adaptive SMC to reduce chatter [43]. An alternative approach to minimizing the chattering consists of optimal gain tuning. There are two common strategies for tuning parameters. The first strategy involves merging multiple objectives into one single objective [44,45]. The second strategy is to utilize multi-objective optimization (MOO) versions of single-objective optimization algorithms to achieve optimal gains. This approach provides a set of optimal solutions, known as the Pareto optimal front, rather than a single unique solution [46,47]. Many MOO methods have been proposed for improving the setting performance of sliding mode gains of dynamical systems using heuristic optimization methods such as the non-dominated sorting genetic algorithm II (NSGA-II) [48], multi-objective differential evolution (MODE) [49], and multi-objective particle swarm optimization (MOPSO) [50]. Laware et al. [46] utilized sliding mode control (SMC) and evolutionary techniques for the level control system. In this paper, the performance of various multi-objective algorithms is compared, and it is shown that the NSGA-II outperforms the other optimization algorithms. Yan et al. [51] proposed an algorithm based on the NSGA-II and an asymmetric sliding mode controller to find a solution for the control problem of connected autonomous vehicles. Rezapour et al. [52] developed a control

schema based on fuzzy sliding mode and genetic algorithms to tune the sliding parameters and find the fuzzy rules. Acharya and Gude [53] implemented an integral sliding mode controller with NSGA-II parameter tuning for a second-order unstable magnetic levitation plant to stabilize the system. Their results demonstrated that the sliding mode controller has superior performance to the proportional-integral-derivative (PID) controller.

Additionally, SMCs also require the availability of full states. Kalman filters and extended Kalman filters (EKFs) have been extensively used in the literature to estimate the unknown states from real-world noisy measurements [54]. Hence, we have also developed an EKF by adapting a recently developed EKF for fuel cells [19] based on a lumped model of the transient pseudo 2D model [18]. As such, this paper will focus on designing a nonlinear controller for power profile tracking of a fuel cell using realistic noisy data and optimizing (minimizing) the settling time, controller chatter, and tracking time. The specific cost functions to achieve these objectives are provided in Section 2.6.

The proposed controller consists of an adaptive SMC to control the duty cycle of the boost convertor. The controller is coupled with an EKF that estimates the internal states of the PEMFC while filtering the measurements. The design of the EKF is presented in Section 2.5.1, while the design and stability analysis are presented in Section 2.5.2. The main contributions of the paper can be summarized as follows:

- Use of accurate dynamics of the fuel cell.
- Development of an SMC controller to control power output.
- Use of the NSGA-II-based algorithm to optimize the SMC hyperparameter.
- Use of an EKF to mitigate the effect of noise.

2. Theoretical approach

2.1. Mathematical modeling of the system

In a normal PEMFC, hydrogen molecules split into two protons and two electrons at the anode. The protons pass through the proton exchange membrane, while the electron travels through an external circuit as current. At the cathode, four protons and four electrons combine with one molecule of oxygen to produce water. A buck-boost converter is used to connect the PEMFC to the load to match the voltage and current requirements. In effect, the specific power output of the cascaded system is controlled to match the desired specific power output of the load. Figure 1 shows the PEMFC system along with the power converter.

2.2. Boost converter modeling

Boost converters are step-up DC-DC power converters used in different power applications. As shown in Figure 1, the converter consists of an inductor (L_C), a capacitor (C_C), a diode, load resistance (R_L), and a pulse width modulation (PWM) generator. Due to the presence of the inductor, the boost converter can convert a low voltage on the fuel cell side V_{cell} to a much higher output voltage V_O. The input of the boost converter is PWM, which is a series of square waves with different duty cycles that switch the boost converter to either on or off. The input of PWM is represented by u.

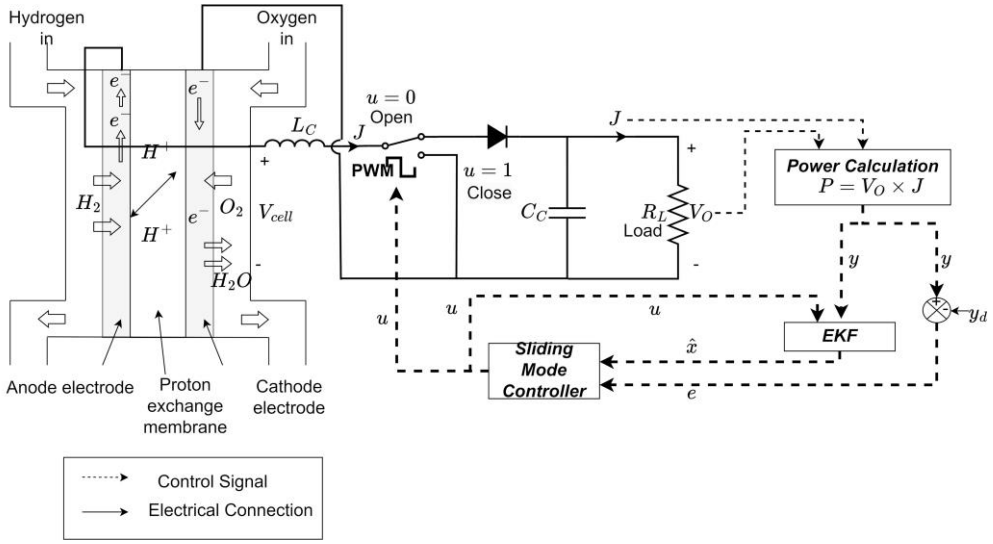

Figure 1. Overall PEMFC power control system configuration.

In order to develop the model of the boost converter, we will assume that the capacitor, inductor, and switches are ideal. We will assume that the switch is able to switch at a sufficiently large frequency. While non-ideal components may reduce the overall conversion efficiencies, converters with nearly 94% efficiency have been developed in the literature [55].

When the switch is open (denoted by $u = 0$), the PEMFC is connected to the load. By considering an additive noise added to the dynamics in the literature [56,57], when the switch is open,

$$\dot{J}\big|_{u=0} = \frac{V_{cell}}{A_{fc}L_C} - \frac{V_O}{A_{fc}L_C} + w_J, \tag{1}$$

$$\dot{V}_O\big|_{u=0} = \frac{A_{fc}J}{C_C} - \frac{V_O}{C_C R_L} + w_{V0}, \tag{2}$$

When the switch is in the closed position (denoted by $u = 1$), the PEMFC is disconnected from the load and is only connected to the inductor. Here, the dynamical equations can be rewritten as follows:

$$\dot{J}\big|_{u=1} = \frac{V_{cell}}{A_{fc}L_C} + \frac{w_J}{A_{fc}}, \tag{3}$$

$$\dot{V}_O\big|_{u=1} = -\frac{V_O}{C_C R_L} + w_{V0}, \tag{4}$$

Hence, using the average method [58], the state-space modeling of the boost converter can be determined as follows:

$$\dot{J} = (1-u)\dot{J}\big|_{u=0} + u\dot{J}\big|_{u=1} = \frac{V_{cell} - V_O}{A_{fc}L_C} + \frac{V_o}{A_{fc}L_C}u, \tag{5}$$

$$\dot{V}_O = (1-u)\dot{V}_O\big|_{u=0} + u\dot{V}_O\big|_{u=1} = \frac{A_{fc}J}{C_C} - \frac{V_O}{C_C R_L} - \frac{A_{fc}J}{C_C}u + w_{V0}, \tag{6}$$

where $u \in [0\ 1]$ is the PWM duty cycle.

2.3. PEMFC modeling

This subsection, develops the state-space model of the fuel cell using the model previously developed in Vijayaraghavan et al. [59] and Romey et al. [19]. The model assumes that the fuel cell can be modeled using lumped parameters. The lumped mode has been previously found to deviate by less than 5% [60].

The closed-circuit voltage of a fuel cell under load is calculated by subtracting the ohmic voltage loss (V_{ohm}) and the activation overpotential ($V_{act,DL}$) from the open-circuit voltage. Thus,

$$V_{cell} = E_{cell} - V_{ohm} - V_{act,DL}, \tag{7}$$

V_{ohm} can be calculated by following [3,61,62]:

$$V_{ohm} = JA_{fc}\left(\rho_0 + \rho_J A_{fc} J + \rho_T\left(T_{fc} - 298\right)\right), \tag{8}$$

The dynamics of the activation voltage is modeled as a double-layer capacitor in parallel to the activation voltage [3,61,62].

$$C_{DL}\dot{V}_{act,DL} + A_{fc}J_{act} = A_{fc}J, \tag{9}$$

and

$$V_{act,DL} = 2V_{act,0} \times arcsinh\frac{J_{act}}{2J_{O_2-0}}, \tag{10}$$

Taking the derivative of Eq (10),

$$\dot{V}_{act,DL} = 2V_{act,0}\frac{1}{\sqrt{1 + \left(J_{act}/2J_{O_2-0}\right)^2}}\frac{\dot{J}_{act}}{2J_{O_2-0}}, \tag{11}$$

Substituting Eq (11) into Eq (9), we find

$$\dot{J}_{act} = \left(\frac{\sqrt{4J_{O2-0}^2 + J_{act}^2}}{2V_{act,0}}\right)\frac{A_{fc}}{C_{DL}}(J - J_{act}), \tag{12}$$

The electrochemical open-circuit cell voltage can be given by using the Nernst equation [3,61,62]:

$$E_{cell} = E_{0,cell} + B_{conc}\, ln\left[\left(\phi_{H2,eff}\right)^2\left(\phi_{O2,eff}\right)\right], \tag{13}$$

where B_{conc} is the parameter that accounts for effective kinetic reactant concentration and is between 0.03 and 0.06 [63]. It may be noted that Eq (13) takes the effect of the diffusion gradient into account and considers the effective concentrations of H_2 and O_2 at the catalyst rather than the concentrations in the channel. Owing to the faster diffusion rate of hydrogen compared to oxygen, we can neglect the concentration gradient at the cathode, and

$$\phi_{H2,eff} = \phi_{H2-ch} = \phi_{H2,A}^{in}, \tag{14}$$

Since the diffusion coefficients of oxygen and water vapor are nearly equal, the oxygen gradient will be calculated using Fick's first law with an equivalent diffusion coefficient, *D* [18,59].

$$\frac{\partial \phi}{\partial t} = D\frac{\partial^2 \phi}{\partial z^2}, \tag{15}$$

We will set $z = 0$ at the channel and $z = L$ at the catalyst. These yield [3,61,62]

$$\begin{aligned} \phi|_{z=0} &= \phi_{O2-ch}, \\ -D\left.\frac{d\phi}{dz}\right|_{z=L} &= \frac{RTJ_{act}}{4FP_{atm}}, \end{aligned} \tag{16}$$

We can then calculate $\phi_{O2,eff} \coloneqq \phi|_{z=L}$ by considering the first two modes for ϕ_{O2-ch} and the first mode for J_{act} [18,59]:

$$\begin{aligned} \phi_{O2,eff} = &\left(1 - \frac{8}{3\pi}\right) \times \phi_{O2-ch} + \frac{4}{\pi}\frac{1}{s\tau_0 + 1}\phi_{O2-ch} - \frac{4}{3\pi}\frac{1}{s\tau_1 + 1}\phi_{O2-ch} \\ &- \left[\left(1 - \frac{8}{\pi^2}\right)J_{act} + \frac{8}{\pi^2}\frac{1}{s\tau_0 + 1}J_{act}\right] \times \frac{RTL}{4FDP_{atm}}, \end{aligned} \tag{17}$$

We can also calculate the flux of oxygen at the channel, considering the first two modes of J_{act} and ignoring the modes of ϕ_{O2-ch} as [18,59]

$$\begin{aligned} \Gamma_{ch} &\coloneqq -\frac{DP_{atm}}{RT}\left.\frac{d\phi}{dz}\right|_{z=0} \\ &= \frac{1}{4F}\left\{\left(1 - \frac{8}{3\pi}\right)J_{act} + \frac{4}{\pi}\frac{1}{s\tau_0 + 1}J_{act} - \frac{4}{3\pi}\frac{1}{s\tau_1 + 1}J_{act}\right\}, \end{aligned} \tag{18}$$

In the time domain, defining the first two modes for ϕ_{O2-ch} as ϕ_0, ϕ_1 and the first two modes for J_{act} as J_0, J_1,

$$\begin{aligned} \dot{\phi}_0 &= \tau_0^{-1}(\phi_{O2-ch} - \phi_0), \\ \dot{\phi}_1 &= \tau_1^{-1}(\phi_{O2-ch} - \phi_1), \\ \dot{J}_0 &= \tau_0^{-1}(J_{act} - J_0), \\ \dot{J}_1 &= \tau_1^{-1}(J_{act} - J_1), \end{aligned} \tag{19}$$

Defining

$$\begin{aligned} \gamma_{p1} = 1 - \frac{8}{3\pi},\ \gamma_{p2} = \frac{4}{\pi},\ \gamma_{p3} = \frac{4}{3\pi}, \\ \gamma_{J1} = 1 - \frac{8}{\pi^2}, \gamma_{J2} = \frac{8}{\pi^2}, \end{aligned} \tag{20}$$

$\phi_{O2,eff}$ and Γ_{ch} can be written as follows:

$$\begin{aligned} \phi_{O2,eff} = &\gamma_{p1}\phi_{O2-ch} + \gamma_{p2}\phi_0 - \gamma_{p3}\phi_1 \\ &- \left[\gamma_{J1}J_{act} + \gamma_{J2}J_0\right] \times \frac{RT_{fc}L}{4FDP_{atm}}, \end{aligned} \tag{21}$$

$$\Gamma_{ch} = \frac{1}{4F}\left(\gamma_{p1}J_{act} + \gamma_{p2}J_0 - \gamma_{p3}J_1\right), \tag{22}$$

In the above equations, ϕ_{O2-ch} would be the average oxygen concentration in the channel.

$$\phi_{O2-ch} = (1-\zeta)\phi_{O2,C}^{in} + \zeta\phi_{O2,C}^{out}, \tag{23}$$

Since the pressure is constant, we find that $\phi_{O2,C}^{in}$ and $\phi_{O2,C}^{out}$ can be defined as follows:

$$\phi_{O2,C}^{in} = P_C\chi_{O2,C}^{in}, \tag{24}$$

$$\phi_{O2,C}^{out} = P_C\chi_{O2,C}^{out}, \tag{25}$$

where $\chi_{O2,C}^{in}$ and $\chi_{O2,C}^{out}$ are oxygen molar concentrations of oxygen at the cathode inlet and the cathode outlet, respectively. If we consider the total molar flow rate to be $\dot{N}_c$,

$$\chi_{O2,C}^{in} = \frac{\dot{N}_{O2,C}^{in}}{\dot{N}_C}, \tag{26}$$

For an oxygen flux Γ_{ch}, $A_{fc}\,\Gamma_{ch}$ mole per second of oxygen would be removed, producing $2A_{fc}\Gamma_{ch}$ moles per second of water. Hence, at the outlet,

$$\chi_{O2,C}^{out} = \frac{\chi_{O2,C}^{in}\,\dot{N}_c - A_{fc}\,\Gamma_{ch}}{\dot{N}_c + A_{fc}\Gamma_{ch}}, \tag{27}$$

Substituting Eqs (26) and (27) into Eqs (24) and (25), and using Eq (23), we find

$$\phi_{O2-ch} = \phi_{O2,C}^{in} - \zeta\frac{\left(P_c + \phi_{O2,C}^{in}\right)A_{fc}\,\Gamma_{ch}}{\left(\dot{N}_c + A_{fc}\Gamma_{ch}\right)}, \tag{28}$$

2.4. The overall model of the cascaded system

The overall system can be modeled using Eqs (5), (6), (12), and (20), with the fuel cell voltage given by

$$\begin{aligned} V_{cell} = \quad & E_{0,cell} + B_{conc}\,ln\left[\left(\phi_{H2,A}^{in}\right)^2\left(\phi_{O2,eff}\right)\right] \\ & - JA_{fc}\left(\rho_0 + \rho_J A_{fc} J + \rho_T\left(T_{fc} - 298\right)\right) \\ & - 2\,V_{act,0} \times arcsinh\left(\frac{J_{act}}{2J_{O2-0}}\right), \end{aligned} \tag{29}$$

and ϕ_{O2-ch} is given by Eq (21).

The specific power output of the system is given by

$$y = V_O J + v, \tag{30}$$

In the state space form considering noise, the model can be written as

$$\dot{x} = \mathcal{F}(x,u,w) = f(x) + g_u(x)u + g_w(x)w, \tag{31}$$

$$y = \mathcal{H}(x,u,v) = \ h(x) + v, \tag{32}$$

where $x = [\phi_0, \phi_1, J_0, J_1, J_{act}, J, V_O]^T$, $w = [w_J, w_{V0}]$, and

$$f = \begin{bmatrix} \tau_0^{-1}(\phi_{O2-ch} - x_1) \\ \tau_1^{-1}(\phi_{O2-ch} - x_2) \\ \tau_0^{-1}(J_{act} - x_3) \\ \tau_1^{-1}(J_{act} - x_4) \\ \frac{\sqrt{4J_{O2-0}^2 + x_5^2}}{2V_{act,0}C_{DL}/A_{fc}}(x_6 - x_5) \\ \frac{V_{cell} - x_6}{L_C} \\ \frac{x_6}{C_C} - \frac{x_7}{C_C R_L} \end{bmatrix}, g_u = \begin{bmatrix} 0 \\ 0 \\ 0 \\ 0 \\ 0 \\ \frac{x_7}{L_C} \\ -\frac{x_6}{C_C} \end{bmatrix}, g_w = \begin{bmatrix} 0 & 0 \\ 0 & 0 \\ 0 & 0 \\ 0 & 0 \\ 1 & 0 \\ 0 & 1 \end{bmatrix},$$
$$h(x, v) = x_6 x_7, \tag{33}$$

2.5. Extended Kalman filter-based nonlinear controller design

As discussed earlier, this paper aims to optimally track specific power profiles using a sliding mode controller. To this end, the design will minimize settling time, controller chatter, and tracking time. The specific cost functions to achieve these objectives are provided in Section 2.6. In the real world, the fuel cell is subject to disturbances, and measurements are subject to noise. Hence, we will use an extended Kalman filter to both filter the measurements and to estimate unmeasured states. The estimated states will then be used to implement a nonlinear sliding mode controller.

2.5.1. Observer design

We will construct the state estimator as

$$\dot{\hat{x}} = \mathcal{F}(\hat{x}, u, 0) - L\big(y - \mathcal{H}(\hat{x}, u, 0)\big), \tag{34}$$

Defining the state estimation error as $\tilde{x} \coloneqq x - \hat{x}$, we find

$$\dot{\tilde{x}} = \mathcal{F}(x, u, w) - \mathcal{F}(\hat{x}, u, 0) + L\big(\mathcal{H}(x, u, v) - h(\hat{x}, u, 0)\big), \tag{35}$$

Taking the first-order approximation of the error dynamics about $\hat{x}$, the dynamics can be approximated as

$$\dot{\tilde{x}} = (A - LC)\tilde{x} + B_W w + L D_v v, \tag{36}$$

where

$$A = \frac{\partial \mathcal{F}}{\partial x}\Big|_{\hat{x},u,w=0}, B_w = \frac{\partial \mathcal{F}}{\partial w}\Big|_{\hat{x},u,w=0}, C = \frac{\partial \mathcal{H}}{\partial x}\Big|_{\hat{x},u,v=0}, \quad D_v = \frac{\partial \mathcal{H}}{\partial v}\Big|_{\hat{x},u,v=0}, \tag{37}$$

The observer gain, L, will be calculated by solving the following Riccati equation arising from the extended Kalman filter:

$$\dot{P} = AP + PA^T - PC^T(D_v R_v D_v^T)^{-1} CP + B_w Q_w B_w^T, \tag{38}$$

$$= PC^T(D_v R_v D_v^T)^{-1}, \tag{39}$$

where P is the covariance estimation of error, Q_w and R_v are the effective covariance of w and v, respectively.

We will now calculate the matrices.

$$C = \frac{\partial(y)}{\partial x} = [0 \quad 0 \quad 0 \quad 0 \quad 0 \quad x_7 \quad x_6], \tag{40}$$

$D_v = 1$, and for $w = \left[w_{V0}, w_J\right]^T$,

$$B_w = \frac{\partial \mathcal{F}}{\partial w} = \begin{bmatrix} 0 & 0 \\ 0 & 0 \\ 0 & 0 \\ 0 & 0 \\ 1 & 0 \\ 0 & 1 \end{bmatrix}, \tag{41}$$

We will now calculate the required partial derivatives for A. From Eq (28),

$$\begin{aligned} \frac{\partial \phi_{O2-ch}}{\partial x} &= -\zeta \frac{\partial}{\partial x}\left[\frac{\left(P_c + \phi_{O2,C}^{in}\right)}{\left(\dot{N}_c\left(A_{fc}\Gamma_{ch}\right)^{-1} + 1\right)}\right] \\ &= -\zeta \frac{\left(P_c + \phi_{O2,C}^{in}\right)}{\left(\dot{N}_c\left(A_{fc}\Gamma_{ch}\right)^{-1} + 1\right)^2} \frac{\dot{N}_c}{A_{fc}\Gamma_{ch}^2} \frac{\partial \Gamma_{ch}}{\partial x}, \end{aligned} \tag{42}$$

Simplifying Eq (42) and substituting for $\partial\Gamma_{ch}/\partial x$ by taking the derivative of Eq (22), we find

$$\frac{\partial \phi_{O2-ch}}{\partial x} = -\zeta \frac{\left(P_c + \phi_{O2,C}^{in}\right) A_{fc}\dot{N}_c}{4F\left(\dot{N}_c + A_{fc}\Gamma_{ch}\right)^2} [0 \quad 0 \quad \gamma_{p2} \quad -\gamma_{p3} \quad \gamma_{p1} \quad 0 \quad 0], \tag{43}$$

Hence, for the first two rows of $\mathcal{F}$,

$$\begin{aligned} \frac{\partial}{\partial x}\begin{bmatrix} \mathcal{F}_1 \\ \mathcal{F}_2 \end{bmatrix} = -\zeta \frac{\left(P_c + \phi_{O2,C}^{in}\right) A_{fc}\dot{N}_c}{4F\left(\dot{N}_c + A_{fc}\Gamma_{ch}\right)^2} &[0 \quad 0 \quad \gamma_{p2} \quad -\gamma_{p3} \quad \gamma_{p1} \quad 0 \quad 0] \\ &\times \begin{bmatrix} \tau_0^{-1} \\ \tau_1^{-1} \end{bmatrix} + \begin{bmatrix} -\tau_0^{-1} & 0 & 0 & 0 & 0 & 0 \\ 0 & -\tau_1^{-1} & 0 & 0 & 0 & 0 \end{bmatrix}, \end{aligned} \tag{44}$$

The partial derivative of $\mathcal{F}_5$ is given as follows.

$$\frac{\partial \mathcal{F}_5}{\partial x} = \begin{bmatrix} 0 & 0 & 0 & 0 & -\tau_{act_{ef}}^{-1} & \tau_{act}^{-1} & 0 \end{bmatrix}, \tag{45}$$

where

$$\tau_{act_{ef}}^{-1} := \frac{4\,J_{O2-0}^2 + (J_{act})^2 - J \times J_{act}}{2\,V_{act,0} C_{DL}/A_{fc}\sqrt{4\,J_{O2-0}^2 + (J_{act})^2}},$$

$$\tau_{\text{act}}^{-1} := \frac{\sqrt{4\,J_{O2-0}^2 + (J_{act})^2}}{2\,V_{act,0} C_{DL}/A_{fc}},$$

Calculating the derivative of $\phi_{O2,eff}$ from Eq (21), and substituting for $\partial\phi_{O2-ch}/\partial x$ from Eq (43),

$$\begin{aligned}\frac{\partial \phi_{O2,eff}}{\partial x} = -\gamma_{p1}\frac{\left(P_c + \phi_{O2,C}^{in}\right)A_{fc}\dot{N}_c}{4F\left(\dot{N}_c + A_{fc}\,\Gamma_{ch}\right)^2}[0 \quad 0 \quad \gamma_{p2} \quad -\gamma_{p3} \quad \gamma_{p1} \quad 0 \quad 0] \\ + \left[\gamma_{p2} \quad -\gamma_{p3} \quad -\gamma_{J2}\frac{RTL}{4FDP_{atm}} \quad 0 \quad -\gamma_{J1}\frac{RTL}{4FDP_{atm}} \quad 0 \quad 0\right],\end{aligned} \tag{46}$$

Calculating $\partial V_{cell}/\partial x$ from Eq (29), and substituting for $\partial\phi_{O2,eff}/\partial x$ from Eq (46),

$$\begin{aligned}\frac{\partial (V_{cell})}{\partial x} = \frac{-B_{comc}}{\phi_{O2,eff}}\gamma_{p1}\frac{\left(P_c + \phi_{O2,C}^{in}\right)A_{fc}\dot{N}_c}{4F\left(\dot{N}_c + A_{fc}\,\Gamma_{ch}\right)^2} \\ \times [0 \quad 0 \quad \gamma_{p2} \quad -\gamma_{p3} \quad \gamma_{p1} \quad 0 \quad 0] \\ + \frac{B_{comc}}{\phi_{O2,eff}}\left[\gamma_{p2} \quad -\gamma_{p3} \quad -\gamma_{J2}\frac{RTL}{4FDP_{atm}} \quad 0 \quad -\gamma_{J1}\frac{RTL}{4FDP_{atm}} \quad 0 \quad 0\right] \\ - A_{fc}\left(\left(\rho_0 + \rho_T\left(T_{fc} - 298\right)\right) + 2J\rho_J A_{fc}\right)[0 \quad 0 \quad 0 \quad 0 \quad 0 \quad 1 \quad 0] \\ - \frac{2\,V_{act,0}(2J_{O2-0})}{\sqrt{4\,J_{O2-0}^2(J_{act})^2 + 1}}[0 \quad 0 \quad 0 \quad 0 \quad 1 \quad 0 \quad 0] \\ := [\gamma_{v1} \quad \gamma_{v2} \quad \gamma_{v3} \quad \gamma_{v4} \quad \gamma_{v5} \quad \gamma_{v6} \quad 0],\end{aligned} \tag{47}$$

where

$$\gamma_{v1} = \frac{B_{comc}}{\phi_{O2,eff}}\,\gamma_{p2},\ \gamma_{v2} = -\frac{B_{comc}}{\phi_{O2,eff}}\,\gamma_{p3},$$

$$\gamma_{v3} = \frac{-B_{comc}}{4F\phi_{O2,eff}}\left[\frac{\gamma_{p1}\gamma_{p2}\left(P_c + \phi_{O2,C}^{in}\right)A_{fc}\dot{N}_c}{\left(\dot{N}_c + A_{fc}\,\Gamma_{ch}\right)^2} + \frac{\gamma_{J2}RTL}{DP_{atm}}\right],$$

$$\gamma_{v4} = \frac{\gamma_{p1}\gamma_{p3}B_{comc}}{4F\phi_{O2,eff}}\frac{\left(P_c + \phi_{O2,C}^{in}\right)A_{fc}\dot{N}_c}{\left(\dot{N}_c + A_{fc}\,\Gamma_{ch}\right)^2}, \tag{48}$$

$$\gamma_{v5} = \frac{-B_{comc}}{4F\phi_{O2,eff}}\left[\gamma_{p1}^2\frac{\left(P_c + \phi_{O2,C}^{in}\right)A_{fc}\dot{N}_c}{\left(\dot{N}_c + A_{fc}\,\Gamma_{ch}\right)^2} + \gamma_{J1}\frac{RTL}{DP_{atm}}\right] - \frac{2\,V_{act,0}(2J_{O2-0})}{\sqrt{4\,J_{O2-0}^2(J_{act})^2 + 1}},$$

$$\gamma_{v6} = -A_{fc}\left(\rho_0 + \rho_T\left(T_{fc} - 298\right) + 2J\rho_J A_{fc}\right),$$

Hence,

$$A = \frac{\partial \mathcal{F}(x,J)}{\partial x} = \begin{bmatrix} \begin{bmatrix} -\tau_0^{-1} & 0 & \tau_\phi\,\gamma_{p2} & -\tau_\phi\,\gamma_{p3} & \tau_\phi\,\gamma_{p1} & 0 & 0 \\ 0 & -\tau_1^{-1} & \tau_\phi\,\gamma_{p2} & -\tau_\phi\,\gamma_{p3} & \tau_\phi\,\gamma_{p1} & 0 & 0 \\ 0 & 0 & -\tau_0^{-1} & 0 & \tau_0^{-1} & 0 & 0 \\ 0 & 0 & 0 & -\tau_1^{-1} & \tau_1^{-1} & 0 & 0 \\ 0 & 0 & 0 & 0 & -\tau_{act_{ef}}^{-1} & \tau_{act}^{-1} & 0 \end{bmatrix} \\ A_{fc}L_C^{-1}([\,\gamma_{v1} \quad \gamma_{v2} \quad \gamma_{v3} \quad \gamma_{v4} \quad \gamma_{v5} \quad \gamma_{v6} \quad (1-u)]) \\ C_C^{-1}\begin{bmatrix} 0 & 0 & 0 & 0 & 0 & A_{fc}(1-u) & R_L^{-1} \end{bmatrix} \end{bmatrix}, \tag{49}$$

2.5.2. Nonlinear controller design

The controller will be designed to be Lyapunov stable. To that end, we will now provide a few definitions and derivations needed to prove stability.

Definition 1 [64]: A continuous function $\eta: [0, a) \mapsto [0, \infty)$ for $a \in (0, \infty)$ is called the $\mathcal{K}$ function, if it is continuously increasing, $\eta(0) = 0$, and $\lim_{\bar{x}\to a, a\to\infty} \eta(\bar{x}) \to \infty$.

A continuous function $\eta: [0, a) \mapsto [0, \infty)$ for $a \in (0, \infty)$ is called the $\mathcal{L}$ function, if it is continuously decreasing and $\lim_{\bar{x}\to a, a\to\infty} \eta(\bar{x}) \to 0$.

A continuous function $\eta(\bar{x}_1, \bar{x}_2)$ is called the $\mathcal{KL}$ function, if for a constant $\bar{x}_1$, $\eta(\bar{x}_1, \bar{x}_2)$ is a class of the $\mathcal{K}$ function with respect to $\bar{x}_2$, and if for a constant $\bar{x}_2$, $\eta(\bar{x}_1, \bar{x}_2)$ is a class of the $\mathcal{L}$ function with respect to $\bar{x}_1$.

Definition 2 [64]: The nonlinear dynamical system given by Eq (31) is said to be input-to-state stable if for every $x_0 \in \mathbb{R}^n$and every continuous and bounded input $u(t) \in \mathbb{R}^m$, $t \geq 0$, the following solution $x(t)$, $t \geq 0$, of Eq (31) exists and is satisfied.

$$\|x(t)\| \leq \eta_C(\|x_0\|, t) + \gamma_C\left(\sup_{0\leq\tau<t} u(\tau)\right), \tag{50}$$

where $\eta_C(s, t)$, for positive s, is a class $\mathcal{KL}$ function and $\gamma_C(s)$, for positive s, is a class $\mathcal{K}$ function. The input-to-state inequality guarantees that for a bounded input $u(t) \in \mathbb{R}^m$, $t \geq 0$, the state $x(t)$, $t \geq 0$, remains bounded.

Definition 3 [64]: The gradients of$\Psi(x)$ are defined as follows:

$$\nabla_x \Psi(x) = \begin{bmatrix} \frac{\partial \Psi}{\partial x_1} \\ \frac{\partial \Psi}{\partial x_2} \\ \vdots \\ \frac{\partial \Psi}{\partial x_n} \end{bmatrix}, \tag{51}$$

$$\nabla_{xx}\Psi(x) = \begin{bmatrix} \frac{\partial^2\Psi}{\partial x_1^2} & \frac{\partial^2\Psi}{\partial x_1 \partial x_2} & \vdots & \frac{\partial^2\Psi}{\partial x_1 \partial x_n} \\ \frac{\partial^2\Psi}{\partial x_2 \partial x_1} & \frac{\partial^2\Psi}{\partial x_2^2} & \vdots & \frac{\partial^2\Psi}{\partial x_n \partial x_n} \\ \cdots & \cdots & \ddots & \vdots \\ \frac{\partial^2\Psi}{\partial x_n \partial x_1} & \frac{\partial^2\Psi}{\partial x_n \partial x_2} & \cdots & \frac{\partial^2\Psi}{\partial x_n^2} \end{bmatrix}, \tag{52}$$

We will now develop a sliding mode feedthrough controller. First, the tracking error is defined as

$$e = y - y_d, \tag{53}$$

For the sliding surface [65,66], we will use

$$s = k_p e + k_d \dot{e} + k_i \int_0^t e d\tau, \tag{54}$$

We will now show the stability of the system when we choose a control to drive $s \to 0$.

Notice that due to the integral term, if $e \neq 0$, $s \neq 0$. Hence, the convergence of the sliding surface Eq (54) leads to the tracking error Eq (53) becoming zero. Differentiating Eq (54), one obtains

$$\dot{s} = k_p \dot{e} + k_d \ddot{e} + k_i e, \tag{55}$$

Therefore, the condition of $\dot{s} = 0$ is the necessary condition for keeping the tracking error at zero. The first- and second-order derivatives of the tracking error Eq (53) are given by

$$\dot{e} = \dot{y} - \dot{r} = \nabla_x^T h(x)[f(x) + g_u(x)u + g_w(x)w] - \dot{y}_d, \tag{56}$$

$$\begin{aligned} \ddot{e} &= \nabla_x^T h(x)[\nabla_x^T f(x) + \nabla_x^T g_u(x)u + \nabla_x^T g_w(x)w]\dot{x} \\ &\quad + \nabla_x^T h(x)[g_u(x)\dot{u} + g_w(x)\dot{w}] + \\ &\quad [f(x) + g_u(x)u + g_w(x)w]^T \nabla_{xx} h(x)[f(x) + g_u(x)u + g_w(x)w] \\ &\quad - \ddot{y}_d \\ &= \nabla_x^T h(x)[\nabla_x^T f(x) + \nabla_x^T g_u(x)u]\dot{x} + \nabla_x^T h(x)[g_u(x)\dot{u} + g_w(x)\dot{w}] \\ &\quad + [f(x) + g_u(x)u + g_w(x)w]^T \nabla_{xx} h(x)[f(x) + g_u(x)u + g_w(x)w] \\ &\quad - \ddot{y}_d, \end{aligned} \tag{57}$$

Let us consider $g_w(x)$ as given in Eq (33). Substituting for $e, \dot{e}$, and $\ddot{e}$ from Eqs (53), (56), and (57), respectively, into Eq (55), one can find

$$\begin{aligned} \dot{s} &= k_p[\nabla_x^T h(x)\dot{x} - \dot{y}_d] + k_d \nabla_x^T h(x)[\nabla_x^T f(x) + \nabla_x^T g_u(x)u]\dot{x} \\ &\quad + k_d\left[f\left(x(t)\right) + g_u(x)u + w_u\right]^T \nabla_{xx} h(x)\left[f\left(x(t)\right) + g_u(x)u + w_u\right] \\ &\quad + k_d[\nabla_x^T h(x)[g_u(x)\dot{u} + \dot{w}] - \ddot{y}_d] + k_i(h(x) - y_d), \end{aligned} \tag{58}$$

Substituting for $\dot{x}$ from Eq (31) into (58), we find

$$\begin{aligned}\dot{s} = {} & k_p[\nabla_x^T h(x)[f(x) + g(x)u + w_u] - \dot{y}_d] \\ & + k_d \nabla_x^T h(x)[\nabla_x^T f(x) + \nabla_x^T g(x)u][f(x) + g(x)u + w_u] \\ & + k_d\left[f\left(x(t)\right) + g(x)u + w_u\right]^T \nabla_{xx} h(x)\left[f\left(x(t)\right) + g(x)u + w_u\right] \\ & + k_d[\nabla_x^T h(x)g(x)\dot{u} + \nabla_x^T h(x)\dot{w}_u - \ddot{y}_d] + k_i(h(x) - y_d),\end{aligned} \tag{59}$$

The controller will be decomposed into u_{eq} and u_s with

$$u = u_{eq} + u_s, \tag{60}$$

It may be noted that $\dot{s} = 0$ is a necessary condition for the error states to converge to zero. As such, the component u_{eq} is the control signal needed to ensure $\dot{s} = 0$ (in the absence of $\dot{u}_s$ and w_u), and is known as the equivalent controller [65–69]. By setting $\dot{s} = 0$, $\dot{u}_s = 0$, and $w_u = 0$ in Eq (59), we obtain [65,69]

$$\begin{aligned}\dot{u}_{eq} = {} & -\left(\nabla_x^T h(x)g(x)\right)^{-1}\{k_p k_d^{-1}[\nabla_x^T h(x)[f(x) + g(x)u] - \dot{y}_d] \\ & + \nabla_x^T h(x)[\nabla_x^T f(x) + \nabla_x^T g(x)u][f(x) + g(x)u] \\ & + [f(x) + g(x)u]^T \nabla_{xx} h(x)[f(x) + g(x)u] \\ & - \ddot{y}_d + k_i k_d^{-1}(h(x) - y_d)\},\end{aligned} \tag{61}$$

The component u_s is referred to as a switching controller and is the component needed to drive s toward $s = 0$. This is known as the reaching condition [66].

$$\begin{aligned}\dot{u}_s = {} & -k_d^{-1}\left(\nabla_x^T h(x)g\left(x(t)\right)\right)^{-1} \times \\ & [m_1|s|sgn(s) + \delta sgn(s) + m_2|s|^{\alpha} sgn(s)],\end{aligned} \tag{62}$$

where m_1 and m_2 are positive, $0 < \alpha < 1$, and $\delta \geq |s| + |k_p w_u + k_d \dot{w}_u|$. In this formula, $sgn(s)$ makes the controller schema discontinuous, but because two integrations are performed, the final controller law is continuous and chattering-free. We need to calculate $\nabla_x f(x)$, $\nabla_x g(x)$, $\nabla_x h(x)$, and $\nabla_{xx} h(x)$ to find $\dot{u}_{eq}$ and $\dot{u}_s$ from Eqs (61) and (62). Notice that

$$\nabla_x f(x) + \nabla_x g(x)u = A, \tag{63}$$

$$\nabla_x h(x) = C, \tag{64}$$

and

$$\nabla_{xx} h(x) = \begin{bmatrix} 0 & 0 & 0 & 0 & 0 & 0 & 0 \\ 0 & 0 & 0 & 0 & 0 & 0 & 0 \\ 0 & 0 & 0 & 0 & 0 & 0 & 0 \\ 0 & 0 & 0 & 0 & 0 & 0 & 0 \\ 0 & 0 & 0 & 0 & 0 & 0 & 0 \\ 0 & 0 & 0 & 0 & 0 & 0 & 1 \\ 0 & 0 & 0 & 0 & 0 & 1 & 0 \end{bmatrix}, \tag{65}$$

Since there is normally an adequate supply of oxygen, we can assume that $\phi_{O2,eff} \neq 0$ and $FDP_{atm} \neq 0$. Hence, $\nabla_x f(x)$ remains bounded (63). Moreover, $\nabla_x g(x)$, $\nabla_x h(x)$, and $\nabla_{xx} h(x)$ are bounded.

Theorem 1: For s, $\dot{u}_{eq}$, and $\dot{u}_s$ as defined in Eqs (54), (61), and (62), respectively, the nonlinear system of the form Eq (31) with bounds

$$\|f(x)\| \leq \mathcal{M}_f, \tag{66}$$

$$\|g_u(x)u\| \leq \mathcal{M}_{g_u}, \tag{67}$$

$$\|g_w(x)\| \leq \mathcal{M}_{g_w}, \tag{68}$$

$$\|\nabla_x f(x) + \nabla_x g(x)u\| \leq \mathcal{M}_{\nabla_x fg}, \tag{69}$$

$$\nabla_x g_{w_i}(x) = 0, \tag{70}$$

$$\|\nabla_x h(x)\| \leq \mathcal{M}_{\nabla_x h}, \tag{71}$$

$$\|\nabla_{xx} h(x)\| \leq \mathcal{M}_{\nabla_{xx} h}, \tag{72}$$

subject to bounded noise considered in Zhu et al. [70].

$$\|w_u\| \leq \mathcal{M}_{w_u}, \|\dot{w}_u\| \leq \mathcal{M}_{\dot{w}_u}, \tag{73}$$

will be driven to the surface $s = 0$ for a sufficiently large δ.

Proof: Consider the candidate Lyapunov function

$$V_1 = \frac{1}{2}s^2, \tag{74}$$

The first derivative of V_1 yields

$$\dot{V}_1 = s\dot{s}, \tag{75}$$

By substituting $\dot{u} = \dot{u}_{eq} + \dot{u}_S$ into Eq (59),

$$\begin{aligned}\dot{s} = {} & k_p[\nabla_x^T h(x)[f(x) + g(x)u + w_u] - \dot{y}_d] \\ & + k_d \nabla_x^T h(x)[\nabla_x^T f(x) + \nabla_x^T g(x)u][f(x) + g(x)u + w_u] \\ & + k_d\big[f\big(x(t)\big) + g(x)u + w_u\big]^T \nabla_{xx} h(x)\big[f\big(x(t)\big) + g(x)u + w_u\big] \\ & + k_d\big[\nabla_x^T h(x)g(x)\big(\dot{u}_{eq} + \dot{u}_S\big) + \nabla_x^T h(x)\dot{w}_u - \ddot{y}_d\big] + k_i(h(x) - y_d),\end{aligned} \tag{76}$$

or

$$\begin{aligned}\dot{s} = {} & k_p[\nabla_x^T h(x)[f(x) + g(x)u] - \dot{y}_d] \\ & + k_d \nabla_x^T h(x)[\nabla_x^T f(x) + \nabla_x^T g(x)u][f(x) + g(x)u] \\ & + k_d\big[f\big(x(t)\big) + g(x)u\big]^T \nabla_{xx} h(x)\big[f\big(x(t)\big) + g(x)u\big] - k_d \ddot{y}_d \\ & + k_{\ i}(h(x) - y_d) + k_d \nabla_x^T h(x) g\big(x(t)\big)\dot{u}_{eq} \\ & + k_d \nabla_x^T h(x)\dot{w}_u + k_p[\nabla_x^T h(x)w_u] \\ & + k_d \nabla_x^T h(x)[\nabla_x^T f(x) + \nabla_x^T g(x)u]w_u \\ & + k_d w_u^T \nabla_{xx} h(x)\big[f\big(x(t)\big) + g(x)u + w_u\big] \\ & + k_d\big[f\big(x(t)\big) + g(x)u + w_u\big]^T \nabla_{xx} h(x)w_u \\ & + k_d w_u^T \nabla_{xx} h(x)w_u + k_d \nabla_x^T h(x)g(x)\dot{u}_S,\end{aligned} \tag{77}$$

Using Eq (61) in (77),

$$\begin{aligned}\dot{s} = {} & k_d \nabla_x^T h(x) \dot{w}_u + k_p [\nabla_x^T h(x) w_u] \\ & + k_d \nabla_x^T h(x) [\nabla_x^T f(x) + \nabla_x^T g(x) u] w_u \\ & + k_d w_u^T \nabla_{xx} h(x) \big[f\big(x(t)\big) + g(x)u + w_u \big] \\ & + k_d \big[f\big(x(t)\big) + g(x)u + w_u \big]^T \nabla_{xx} h(x) w_u \\ & + k_d w_u^T \nabla_{xx} h(x) w_u + k_d \nabla_x^T h(x) g(x) \dot{u}_s,\end{aligned} \tag{78}$$

Using Eq (62), $\dot{s}$ can be written as

$$\begin{aligned}\dot{s} = {} & \big(V_{s_1} + V_{s_2} + V_{s_3} + V_{s_4} + V_{s_5}\big) \\ & - [m_1 |s| sgn(s) + \delta sgn(s) + m_2 |s|^{\alpha} sgn(s)],\end{aligned} \tag{79}$$

where $V_{s_1}, V_{s_2}, V_{s_3}, V_{s_4}$, and V_{s_5} are defined as

$$V_{s_1} = k_d \nabla_x^T h(x) [\nabla_x^T f(x) + \nabla_x^T g(x) u][w_u], \tag{80}$$

$$V_{s_2} = \big(k_d + k_p\big)\big[\nabla_x^T h(x)[w_u]\big], \tag{81}$$

$$V_{s_3} = [\dot{x}_c]^T \nabla_{xx} h(x)[w_u], \tag{82}$$

$$V_{s_4} = [w_u]^T \nabla_{xx} h(x)[\dot{x}_c], \tag{83}$$

$$V_{s_5} = [w_u]^T \nabla_{xx} h(x)[w_u], \tag{84}$$

$$V_{s_6} = \nabla_x^T h(x) \dot{w}_u, \tag{85}$$

Hence, $\dot{V}_1$ is given by

$$\begin{aligned}\dot{V}_1 = {} & s\dot{s} \\ = {} & s\big(V_{s_1} + V_{s_2} + V_{s_3} + V_{s_4} + V_{s_5} + V_{s_6}\big) \\ & + s[m_1 |s| sgn(s) + \delta sgn(s) + m_2 |s|^{\alpha} sgn(s)],\end{aligned} \tag{86}$$

Using (69) for $V_{s_1} = k_d \nabla_x^T h(x) [\nabla_x^T f(x) + \nabla_x^T g(x) u][w_u]$,

$$\begin{aligned}& \nabla_x^T h(x) [\nabla_x^T f(x) + \nabla_x^T g(x) u][w_u] \\ & \quad \leq \|\nabla_x^T h(x)\| \|\nabla_x^T f(x) + \nabla_x^T g(x) u\| \|w_u\| \\ & \quad \leq \mathcal{M}_{\nabla_x h} \mathcal{M}_{\nabla_x f g} \|w_u\|,\end{aligned} \tag{87}$$

Then

$$\begin{aligned}V_{s_1} &= k_d \nabla_x^T h(x) (\nabla_x^T f(x) + \nabla_x^T g(x) u)[w_u] \\ &\leq k_d \big(\mathcal{M}_{\nabla_x h} \mathcal{M}_{\nabla_x f g} \mathcal{M}_{w_u}\big),\end{aligned} \tag{88}$$

Similarly, for $V_{s_2} = \big(k_d + k_p\big)\big[\nabla_x^T h(x)[w_u]\big]$,

$$\|\nabla_x^T h(x)[w_u]\| \leq \left\|\mathcal{M}_{\nabla_x h(x)}\right\|\left\|\mathcal{M}_{w_u}\right\|, \tag{89}$$

For $V_{s_3} = [\dot{x}_c]^T \nabla_{\mathrm{xx}} h(x)[w_u]$, we have

$$V_{s_3} \leq \|\dot{x}_c\|\|\nabla_{xx} h(x)\|\|w_u\|, \tag{90}$$

From Eq (31), $\|\dot{x}_c\| = \|f(x) + g_u(x)u + g_w(x)w\|$ and

$$V_{s_3} \leq \left(\mathcal{M}_f + \mathcal{M}_{g_u} + \mathcal{M}_{g_w}\mathcal{M}_{w_u}\right)\mathcal{M}_{\nabla_{xx}h}\mathcal{M}_{w_u}, \tag{91}$$

Additionally, V_{s_4} is bounded as

$$V_{s_4} \leq \|\dot{x}_c\|\|\nabla_{xx} h(x)\|\|w_u\| \leq \mathcal{M}_{\dot{x}_c}\mathcal{M}_{\nabla_{xx}h}\mathcal{M}_{w_u}, \tag{92}$$

Considering the Cauchy-Schwarz inequality, we have

$$V_{s_5} \leq \|\nabla_{xx} h(x)\|\|w_u\|^2 \leq \mathcal{M}_{\nabla_{xx}h}\mathcal{M}_{w_u}^{\ 2}, \tag{93}$$

and

$$V_{s_6} \leq \|\nabla_x h(x)\|\|\dot{w}_u\| \leq \mathcal{M}_{\nabla_x h}\mathcal{M}_{\dot{w}_u}, \tag{94}$$

Now

$$\begin{aligned}\mathcal{M}_{V_s} \coloneqq\ & \mathcal{M}_{\nabla_x h(x)}\left(\mathcal{M}_{\nabla_x f g} + 1 + \mathcal{M}_{w_u}\right)\mathcal{M}_{w_u} \\ & + 2\mathcal{M}_{\dot{x}_c}\mathcal{M}_{\nabla_{xx}h}\mathcal{M}_{w_u} + \mathcal{M}_{\nabla_{xx}h}\mathcal{M}_{w_u}^{\ 2} + \mathcal{M}_{\nabla_{xx}h}\mathcal{M}_{\dot{w}_u},\end{aligned} \tag{95}$$

Therefore, considering Eqs (86) and (95),

$$\dot{V}_1 \leq \mathcal{M}_{V_s} s + s[m_1|s|sgn(s) + \delta sgn(s) + m_2|s|^{\alpha} sgn(s)], \tag{96}$$

Then

$$\dot{V}_1 \leq \mathcal{M}_{V_s} s - \delta|s| - m_1|s|^2 - m_2|s|^{\alpha+1}, \tag{97}$$

Thus, if the hyperparameter $\delta > \mathcal{M}_{V_s}$, $\dot{V}_1$ is negative for sufficiently large $|s|$. It follows that s is uniformly ultimately bounded. Consequently, we can conclude that the trajectory of error will converge to the origin and the system is stable.

2.6. Hyperparameter optimization

In this sub-section, we implement multi-objective optimizations of the proposed controller. The optimization problem consists of selecting the following six hyperparameters.

$$\theta = \left[k_p, k_d, k_i, \delta, m_1, m_2\right], m_1, m_2 > 0, \tag{98}$$

to simultaneously minimize

$$f_1 = \int_0^T |\dot{u} - \dot{\tilde{u}}|\, dt, f_2 = \int_0^T (e)^2\, dt, f_3 = \int_0^T (\dot{e})^2\, dt, \tag{99}$$

$$f_4 = \int_0^T te^2\, dt, f_5 = \int_0^T |u|\, dt,$$

In the optimization problem, f_1 states the chattering measurement based on [65,71], and shows the difference between the input controller and the nominal value of the input controller. f_2 and f_3 denote the integration of the absolute value of sliding surfaces, and the integration of the derivative of sliding surfaces, respectively. Then, f_4 is the integral of time multiplied by the squared error [72,73] and f_5 is the integral of the absolute value of the input controller. This fitness function is considered to minimize the absolute value of the dissipated energy of the actuators. The optimization constraints are obtained based on the limitation of the designed controller parameters, which is explained in Eq (97). Here, the objective functions, constraints, and variables are defined. To optimize these variables, four benchmarking multi-objective optimization algorithms are considered. In this study, we use the non-dominated sorting genetic algorithm II (NSGA-II) library in MATLAB to perform the gain optimization algorithm for the sliding mode controller. In this algorithm, the individuals are divided into different classes based on their dominance. Therefore, the first class is assigned to the non-dominated individuals, and the following classes are assigned to the individuals who are dominated by the others. When each iteration finishes, the distances among the individuals are computed. The criteria for these distances are known as crowding distances for sorting the individuals. The flowchart of the algorithm is illustrated in Figure 2.

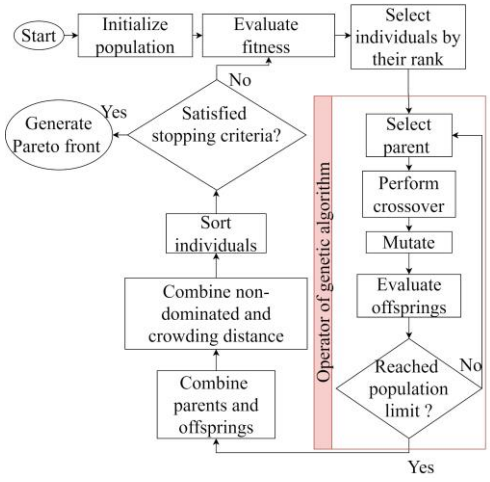

Figure 2. Flowchart of the NSGA-II algorithm for multi-objective optimization.

2.7. Simulation parameters

The PEMFC parameters and the converter parameters used in the study are presented in the symbols table at the beginning of the paper. All simulations used an initial condition $x(t_0) = [0.16,0.16,1,1,1,0,1]^T$ for both the system and the observer.

3. Results and discussion

3.1. Model step response

To better characterize and validate the model developed in Section 2.1, the model response is compared to virtual experiments on the high-fidelity (HF) fuel cell model proposed by Ebrahimi et al. [18] and Vijayaraghavan et al. [59]. The HF model is a transient computational fluid dynamics (CFD) model that has been validated against a Ballard fuel cell. Figure 3 compares the response of the two models to a step change in the current from 50 to 200 A/m^2 at time = 50 s, and shows good agreement between them (with a steady-state difference of $\lesssim$0.1%).

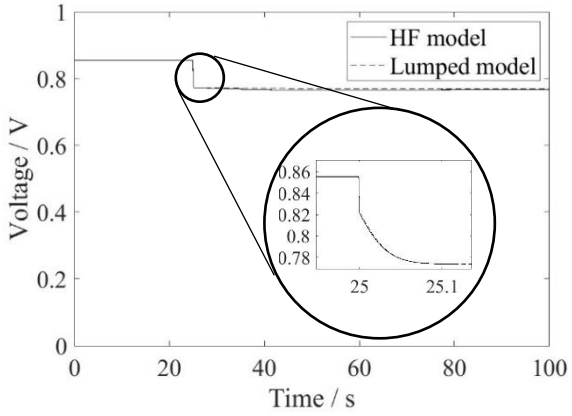

Figure 3. Step response.

3.2. NSGA-II-based optimization

NSGA-II optimization was performed using a maximum number of generations of 100 and a population size of 10 for a sinusoidal desired specific power profile, $5\cos(t) + 3\sin(3t)$. The result of a sample optimization for one of the points on the parent surface is shown in Figure 4. The optimization is seen to converge in 40 generations (before reaching the generation limit). The optimal values of the parameters are found to be $k_p = 1080.9566, k_d = 10.6259, k_i = 0.210,\ \delta = 0.2346, m_2 = 0.4640,$ and $m_2 = 0.4366$. The optimization toolbox in MATLAB R2023 was used to generate the Pareto surface using a Lenovo Y700 with an I7 with 16GB of RAM. The Pareto surface represents a vector optimal solution for a multi-objective optimization problem, wherein no objective functions can be improved in value without degrading other objective values [74]. The optimization procedure returned a 200-point point cloud. As it is rather difficult to visualize the 5-dimensional parent front, we will determine a quadratic polynomial surface fit of the parent front. To this end, we will first scale the fitness function as follows: $\bar{f}_1 = f_1/10^6$, $\bar{f}_2 = f_2/10^5$, $\bar{f}_3 = f_3/10$, $\bar{f}_4 = f_4/10^4$, and $\bar{f}_5 = f_5/10^7$, and perform a regression analysis to fit a quadratic polynomial:

$$\begin{aligned}\bar{f}_5 = k_0 + k_{\bar{f}_1}\bar{f}_1 + k_{\bar{f}_2}\bar{f}_2 + k_{\bar{f}_3}\bar{f}_3 + k_{\bar{f}_4}\bar{f}_4 + k_{\bar{f}_1^2}\bar{f}_1^2 + k_{\bar{f}_2\bar{f}_1}\bar{f}_2\bar{f}_1 \\ + k_{\bar{f}_2^2}\bar{f}_2^2 + k_{\bar{f}_3\bar{f}_1}\bar{f}_3\bar{f}_1 + k_{\bar{f}_3\bar{f}_2}\bar{f}_3\bar{f}_2 + k_{\bar{f}_3^2}\bar{f}_3^2 + k_{\bar{f}_4\bar{f}_1}\bar{f}_4\bar{f}_1 \\ + k_{\bar{f}_4\bar{f}_2}\bar{f}_4\bar{f}_2 + k_{\bar{f}_4\bar{f}_3}\bar{f}_4\bar{f}_3 + k_{\bar{f}_4^2}\bar{f}_4^2 + k_{\bar{f}_5\bar{f}_1}\bar{f}_5\bar{f}_1 + k_{\bar{f}_5\bar{f}_2}\bar{f}_5\bar{f}_2 \\ + k_{\bar{f}_5\bar{f}_3}\bar{f}_5\bar{f}_3 + k_{\bar{f}_5\bar{f}_4}\bar{f}_5\bar{f}_4 + k_{\bar{f}_5^2}\bar{f}_5^2,\end{aligned} \tag{100}$$

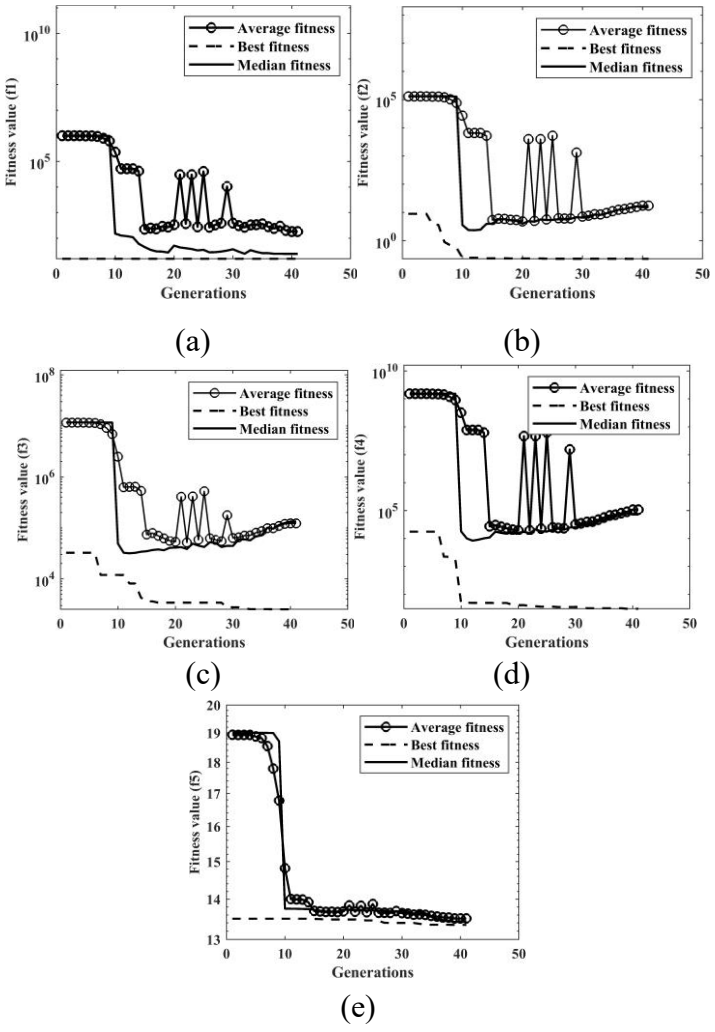

Figure 4. Convergence of multi-objective optimization.

To improve the fitting function, we progressively eliminated the statistically insignificant coefficient of the quadratic polynomial. The final fitting function was found to be

$$\begin{aligned}-0.0236 + 0.6528\,\bar{f}_1 + 0.0592\,\bar{f}_3 + 0.0250\,\bar{f}_4 - \bar{f}_5 + 0.0058\,\bar{f}_1^2 \\ + 7.4778\times10^{-6}\,\bar{f}_2^2 - 0.9045\,\bar{f}_3\bar{f}_1 - 0.0005\,\bar{f}_3\bar{f}_2 - 0.0358\,\bar{f}_3^2 \\ -0.0374\,\bar{f}_4\bar{f}_3 + 6.7997\times10^{-5}\,\bar{f}_4^2 - 0.0090\,\bar{f}_5\bar{f}_1 + 1.4061\,\bar{f}_5\bar{f}_3 = 0,\end{aligned} \tag{101}$$

with a residual error of 3.892×10^{-6}, an R^2 value of 1, and a p-value of $\lesssim 2.2 \times 10^{-16}$ indicating an exceptionally good fit. Figure 5(a) shows a 3D surface plot $\bar{f}_3$ vs. $\bar{f}_4$ vs. $\bar{f}_5$ (with $\bar{f}_1 = 1$ and $\bar{f}_5 = 1$), and Figure 4(b) shows pairwise Pareto curves of different objective functions.

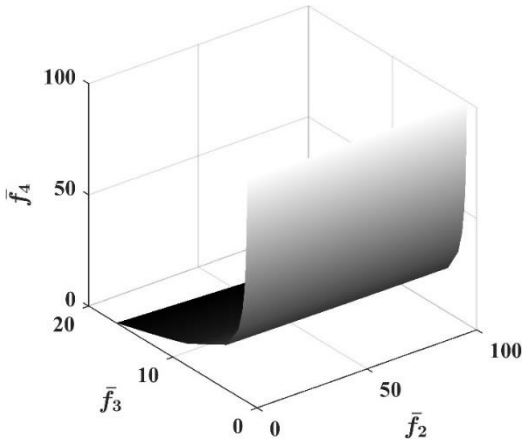

(a) 3D slice of the Pareto surface of $\bar{f}_3$ vs. $\bar{f}_4$ vs. $\bar{f}_5$ (for $\bar{f}_1 = 1$ and $\bar{f}_5 = 1$).

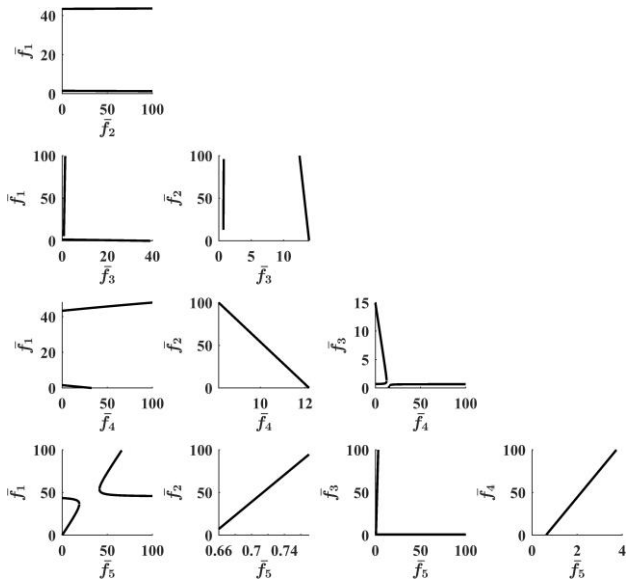

(b) Pairwise 2D Pareto curves of $\bar{f}_i$ vs. $\bar{f}_j$ (with $\bar{f}_k = 1$ for $i, j \neq k$).

Figure 5. Pareto surface.

3.3. Simulation for sinusoidal input

The proposed controller was implemented for the point $k_p = 1080.9566, k_d = 10.6259, k_i = 0.210, \delta = 0.2346, m_2 = 0.4640$, and $m_2 = 0.4366$ on the Pareto surface, and the system and controller were simulated for the desired specific power profile $5\cos(t) + 3\sin(3t)$ on a Lenovo Y700 with an I7 with 16GB of RAM using MATLAB R2023. Figure 6(a) demonstrates that the proposed EKF algorithm can estimate the output in the presence of external disturbances and that the proposed controller can drive the system to the desired power profile trajectory. Therefore, the EKF-based sliding mode controller optimized by the NSGA-II is considered a suitable controller to be used for trajectory tracking. Figure 6(b) depicts the input controller that is used for controlling the specific power of the PEMFC system. This controller schema is designed based on Eqs (61) and (62).

The tracking error in Figure 6(c) and the value of the sliding surface in Figure 6(d) also approach zero over time. There is no overshoot in error, and the system is stabilized in finite time. The integral square error (ISE), integral absolute error (IAE), integral time absolute error (ITAE), and integral time square error (ITSE) of the tracking error are 2488.30, 96.64, 408.69, and 2045.15, respectively.

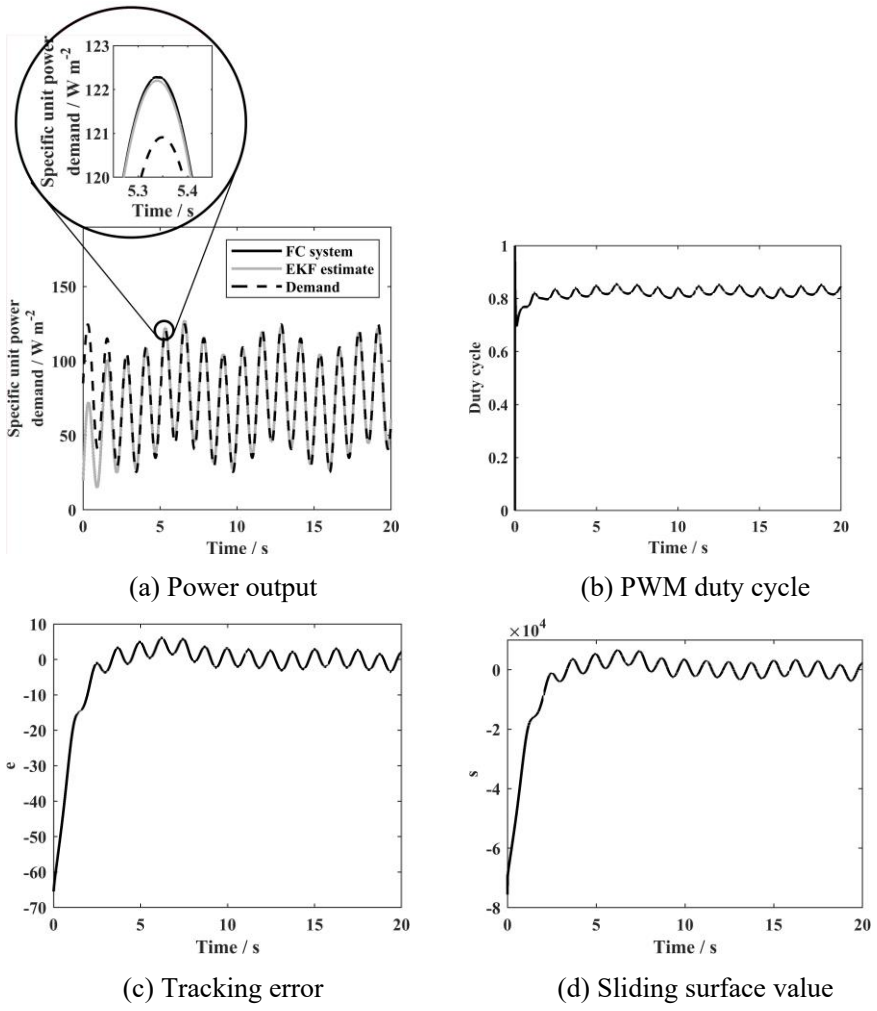

(a) Power output (b) PWM duty cycle

(c) Tracking error (d) Sliding surface value

Figure 6. System response to a sinusoidal target profile.

3.4. Simulation of the system with uncertain parameters

While it may be relatively easier to determine the ohmic parameters, the time constants and limiting current density may have higher uncertainty. As such, the true system model may be different from the nominal model used by the controller. Figure 7 compares the proposed algorithm for different model parameters used by the true system model, while the model used by the controller was fixed ($\tau_0 = 6$ s, $\tau_1 = 0.67$ s, and $J_{lim} = 15000$ A/m^2). The simulation was run on a Samsung Galaxy Book 3 with an I7 with 16GB of RAM using MATLAB R2023. This simulation demonstrates the robustness of the EKF-based SMC to model uncertainties.

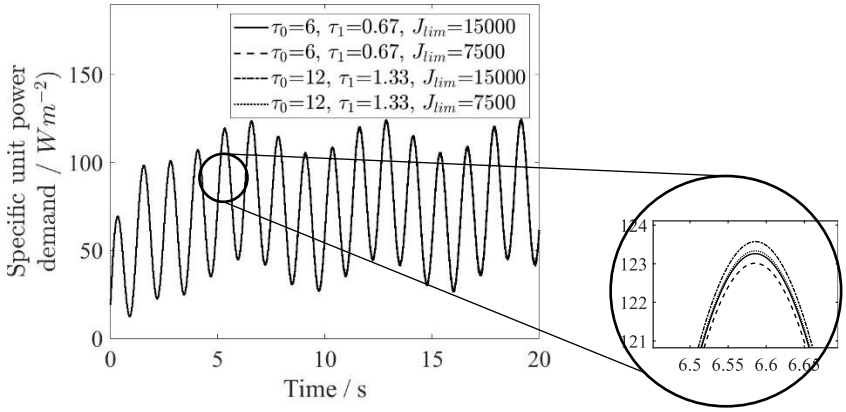

Figure 7. Response of the uncertain system to a sinusoidal target profile.

3.5. Simulation for modified urban dynamometer driving schedule (M-UDDS) input

The (standard) urban dynamometer driving schedule (UDDS) [75] corresponds to driving a vehicle in a typical urban environment and is one of the common driving cycles used for electric vehicles. The M-UDDS was generated by removing the negative power corresponding to the braking action and adding a small constant power to account for the auxiliary power demand. The proposed controller was implemented for the point $k_p = 1080.9566, k_d = 10.6259, k_i = 0.210, \delta = 0.2346, m_2 = 0.4640,$ and $m_2 = 0.4366$ on the Pareto surface, and the system and controller were simulated on a Lenovo Y700 with an I7 with 16GB of RAM using MATLAB R2023 for the M-UDDS cycle. Figure 8(a) shows the power tracking ability of the algorithm for the M-UDDS cycle. It is seen that even though the initial optimization was performed using a sinusoidal profile, the controller can overcome the disturbances and track the desired profile. The controller input signal is depicted in Figure 8(b). This controller signal regards the proposed controller schema that is described in Eqs (61) and (62). Figure 6(c) and (d) illustrate how the suggested algorithm performs in reducing errors. There is no overshoot in error, and the system is stabilized in finite time. The ISE, IAE, ITAE, and ITSE of the tracking error are found to be 13.09, 47.50, 8414.10, and 1867.49, respectively.

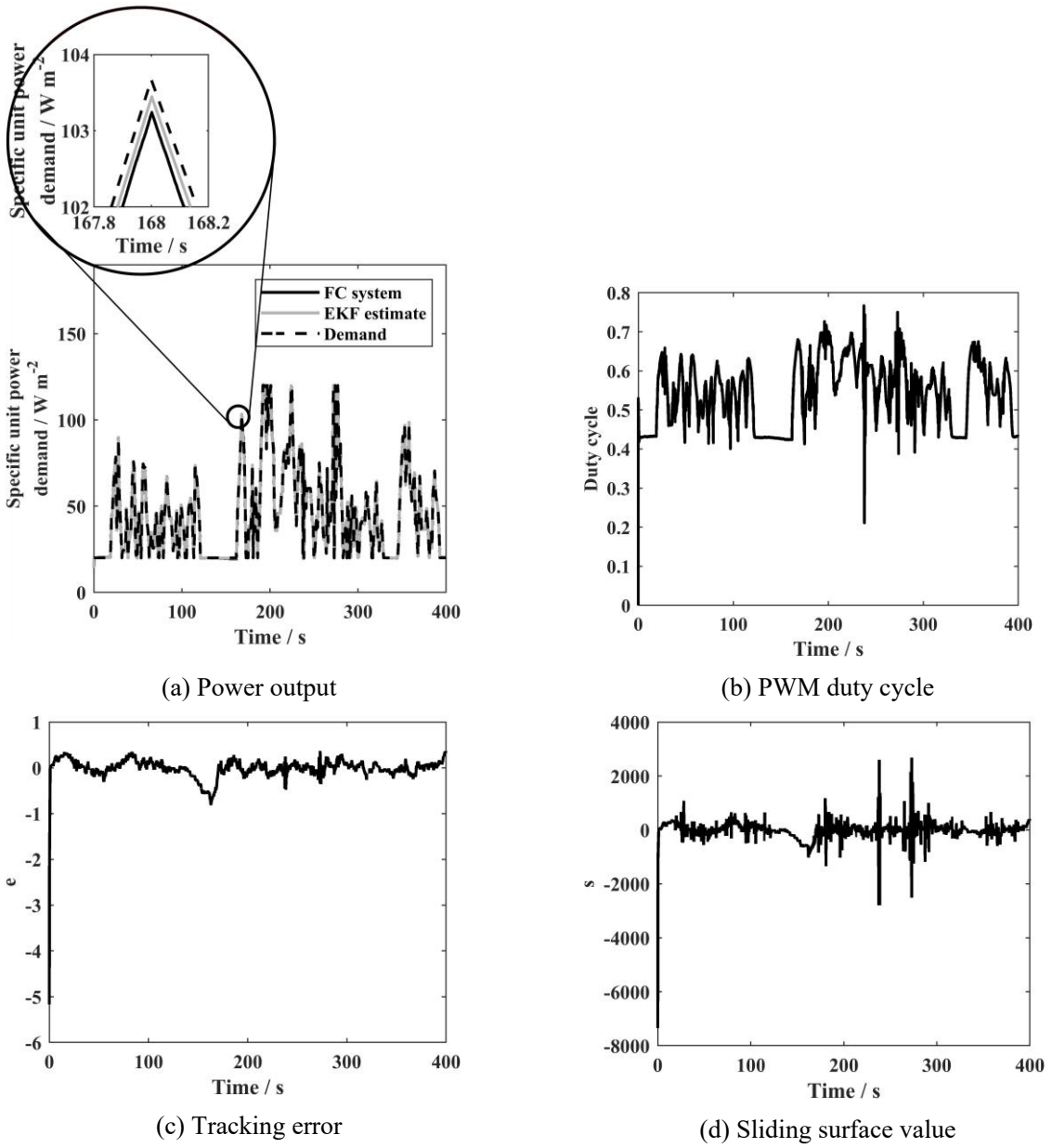

(a) Power output

(b) PWM duty cycle

(c) Tracking error

(d) Sliding surface value

Figure 8. System response to the M-UDDS target profile.

4. Conclusions

This paper has investigated the problem of power tracking control for the PEMFC system feeding a boost converter with noise. A sliding mode control scheme has been presented in detail, and its stability has been proven by applying the Lyapunov theorem. The gains of the controller have been optimized by applying the NSGA-II and designing objective functions to minimize the integral of chattering, the integral absolute value of the sliding surface, the derivative of the sliding surfaces, the input controller, and the time multiplied by squared error. Then, the optimized gains were utilized to show the performance of the proposed controller for three desired specific power profiles: the sine reference signal, the sine reference signal under modeling uncertainties, and the M-UDDS reference

signal. From the simulation study, it was observed that the proposed algorithm's results are satisfactory, and the algorithm can be scaled to a real system.

Use of AI tools declaration

The author declare that they have not used Artificial Intelligence (AI) tools in the creation of this article.

Conflict of interest

The author declare that they do not have any conflict of interest with regards to this paper.

Acknowledgments

The lead author would like to acknowledge the funding from NSERC Discovery Grant (RGPIN-02971) that enabled this research. The authors would also like to thank the anonymous reviewers for their invaluable inputs that help improve the quality of this paper.

Author contributions

Alireza Beigi contributed to the conceptualization, simulation, critical investigation, and writing of the original draft. Dr. Krishna Vijayaraghavan contributed to supervision, writing of original drafts, and incorporating reviewer comments.

References

1. Das PK, Barbir F, Jiao K, et al. (2023) Chapter 1—Fuel cells for transportation—An overview. In: Das PK, Jiao K, Wang Y, et al. (Eds), *Fuel Cells for Transportation*, Woodhead Publishing, 1–28. https://doi.org/10.1016/B978-0-323-99485-9.00013-7
2. Sørensen B, Spazzafumo G (2018) 5—Implementation scenarios. In: Sørensen B, Spazzafumo G (Eds), *Hydrogen and Fuel Cells (Third Edition)*, Academic Press, 273–411. https://doi.org/10.1016/B978-0-08-100708-2.00005-9
3. Barbir F (2005) Chapter 10—Fuel Cell Applications. In: Barbir F (Ed.), *PEM Fuel Cells*, Burlington, Academic Press, 337–397. https://doi.org/10.1016/B978-012078142-3/50011-2
4. Cao Y, Li Y, Zhang G, et al. (2020) An efficient terminal voltage control for PEMFC based on an improved version of whale optimization algorithm. *Energy Rep* 6: 530–542. https://doi.org/10.1016/j.egyr.2020.02.035
5. Li J, Yu T (2021) Distributed deep reinforcement learning for optimal voltage control of PEMFC. *IET Renewable Power Gener* 15: 2778–2798. https://doi.org/10.1049/rpg2.12202
6. Giménez SN, Durá JMH, Ferragud FXB, et al. (2020) Design and experimental validation of the temperature control of a PEMFC stack by applying multiobjective optimization. *IEEE Access* 8: 183324–183343. https://doi.org/10.1109/ACCESS.2020.3029321
7. Huang L, Chen J, Liu Z, et al. (2018) Adaptive thermal control for PEMFC systems with guaranteed performance. *Int J Hydrogen Energy* 43: 11550–11558. https://doi.org/10.1016/j.ijhydene.2017.12.121

8. Segura F, Andujar JM, Duran E (2011) Analog current control techniques for power control in PEM fuel-cell hybrid systems: A critical review and a practical application. *IEEE Trans Ind Electron* 58: 1171–1184. https://doi.org/10.1109/TIE.2010.2049710
9. Garcia-Gabin W, Dorado F, Bordons C (2010) Real-time implementation of a sliding mode controller for air supply on a PEM fuel cell. *J Process Control* 20: 325–336. https://doi.org/10.1016/j.jprocont.2009.11.006
10. Matraji I, Ahmed FS, Laghrouche S, et al. (2015) Comparison of robust and adaptive second order sliding mode control in PEMFC air-feed systems. *Int J Hydrogen Energy* 40: 9491–9504. https://doi.org/10.1016/j.ijhydene.2015.05.090
11. Kakaç S, Pramuanjaroenkij A, Zhou XY (2007) A review of numerical modeling of solid oxide fuel cells. *Int J Hydrogen Energy* 32: 761–786. https://doi.org/10.1016/j.ijhydene.2006.11.028
12. Ghorbani B, Vijayaraghavan K (2019) A review study on software-based modeling of hydrogen-fueled solid oxide fuel cells. *Int J Hydrogen Energy* 44: 13700–13727. https://doi.org/10.1016/j.ijhydene.2019.03.217
13. van Biert L, Godjevac M, Visser K, et al. (2019) Dynamic modelling of a direct internal reforming solid oxide fuel cell stack based on single cell experiments. *Appl Energy* 250: 976–990. https://doi.org/10.1016/j.apenergy.2019.05.053
14. Su Y, Zhong Z, Jiao Z (2022) A novel multi-physics coupled heterogeneous single-cell numerical model for solid oxide fuel cell based on 3D microstructure reconstructions. *Energy Environ Sci* 15: 2410–2424. https://doi.org/10.1039/D2EE00485B
15. Ghorbani B, Vijayaraghavan K (2018) 3D and simplified pseudo-2D modeling of single cell of a high temperature solid oxide fuel cell to be used for online control strategies. *Int J Hydrogen Energy* 43: 9733–9748. https://doi.org/10.1016/j.ijhydene.2018.03.211
16. Javaid U, Iqbal J, Mehmood A, et al. (2022) Performance improvement in polymer electrolytic membrane fuel cell based on nonlinear control strategies—A comprehensive study. *PLoS One* 17: e0264205. https://doi.org/10.1371/journal.pone.0264205
17. Javaid U, Mehmood A, Iqbal J, et al. (2023) Neural network and URED observer based fast terminal integral sliding mode control for energy efficient polymer electrolyte membrane fuel cell used in vehicular technologies. *Energy* 269: 126717. https://doi.org/10.1016/j.energy.2023.126717
18. Ebrahimi S, DeVaal J, Narimani M, et al. (2017) Transient model of oxygen-starved proton exchange membrane fuel cell for predicting voltages and hydrogen emissions. *Int J Hydrogen Energy* 42: 21177–21190. https://doi.org/10.1016/j.ijhydene.2017.05.209
19. Romey W, Vijayaraghavan K (2022) Extended kalman filter for normal and Oxygen-starved PEM fuel cells using a Lumped Pseudo-2D Model. *2022 IEEE International Symposium on Advanced Control of Industrial Processes (AdCONIP)*, 263–268. https://doi.org/10.1109/AdCONIP55568.2022.9894212
20. Park J, Chen Z, Kiliaris L, et al. (2009) Intelligent vehicle power control based on machine learning of optimal control parameters and prediction of road type and traffic congestion. *IEEE Trans Veh Technol* 58: 4741–4756. https://doi.org/10.1109/TVT.2009.2027710
21. Murphey YL, Park J, Chen Z, et al. (2012) Intelligent hybrid vehicle power control—Part I: Machine learning of optimal vehicle power. *IEEE Trans Veh Technol* 61: 3519–3530. https://doi.org/10.1109/TVT.2012.2206064

22. Bahri H, Harrag A (2021) Ingenious golden section search MPPT algorithm for PEM fuel cell power system. *Neural Comput Appl* 33: 8275–8298. https://doi.org/10.1007/s00521-020-05581-4
23. Rafi Kiran S, Altaf M, Sai Niranjan CN, et al. (2023) Design and performance analysis of hybrid optimization MPPT controller for proton exchange membrane fuel cell system with DC-DC converter. *Mater Today: Proc*. https://doi.org/10.1016/j.matpr.2023.07.077
24. Percin HB, Caliskan A (2023) Whale optimization algorithm based MPPT control of a fuel cell system. *Int J Hydrogen Energy* 48: 23230–23241. https://doi.org/10.1016/j.ijhydene.2023.03.180
25. Zhong Z, Huo H, Zhu X, et al. (2008) Adaptive maximum power point tracking control of fuel cell power plants. *J Power Sources* 176: 259–269. https://doi.org/10.1016/j.jpowsour.2007.10.080
26. Lorenz H, Noreikat K-E, Klaiber T, et al. (1997) Method and device for vehicle fuel cell dynamic power control. Available from: https://patents.google.com/patent/US5646852A/en.
27. Mufford WE, Strasky DG (1999) Power control system for a fuel cell powered vehicle. Available from: https://patents.google.com/patent/US5991670A/en.
28. Lauzze KC, Chmielewski DJ (2006) Power control of a polymer electrolyte membrane fuel cell. *Ind Eng Chem Res* 45: 4661–4670. https://doi.org/10.1021/ie050985z
29. Kolavennu PK, Palanki S, Cartes DA, et al. (2008) Adaptive controller for tracking power profile in a fuel cell powered automobile. *J Process Control* 18: 558–567. https://doi.org/10.1016/j.jprocont.2007.10.013
30. Cheng J, Yi J, Zhao D (2007) Design of a sliding mode controller for trajectory tracking problem of marine vessels. *IET Control Theory Appl* 1: 233–237. https://doi.org/10.1049/iet-cta:20050357
31. Elmokadem T, Zribi M, Youcef-Toumi K (2016) Trajectory tracking sliding mode control of underactuated AUVs. *Nonlinear Dyn* 84: 1079–1091. https://doi.org/10.1007/s11071-015-2551-x
32. Chen S-B, Beigi A, Yousefpour A, et al. (2020) Recurrent neural network-based robust nonsingular sliding mode control with input saturation for a non-holonomic spherical robot. *IEEE Access* 8: 188441–188453. https://doi.org/10.1109/ACCESS.2020.3030775
33. Ríos H, Falcón R, González OA, et al. (2019) Continuous sliding-mode control strategies for quadrotor robust tracking: Real-Time application. *IEEE Trans Ind Electron* 66: 1264–1272. https://doi.org/10.1109/TIE.2018.2831191
34. Ali N, Liu Z, Armghan H, et al. (2022) Double integral sliding mode controller for wirelessly charging of fuel cell-battery-super capacitor based hybrid electric vehicle. *J Energy Storage* 51: 104288. https://doi.org/10.1016/j.est.2022.104288
35. Ashok R, Shtessel Y (2015) Control of fuel cell-based electric power system using adaptive sliding mode control and observation techniques. *J Franklin Inst* 352: 4911–4934. https://doi.org/10.1016/j.jfranklin.2015.04.010
36. Moré JJ, Puleston PF, Kunusch C, et al. (2015) Development and implementation of a supervisor strategy and sliding mode control setup for fuel-cell-based hybrid generation systems. *IEEE Trans Energy Convers* 30: 218–225. https://doi.org/10.1109/TEC.2014.2354553
37. Silaa MY, Barambones O, Uralde J, et al. (2025) Simulation and experimental validation of novel sliding mode control with quick power reaching law for a proton exchange membrane fuel cell system. *J Power Sources* 653: 237632. https://doi.org/10.1016/j.jpowsour.2025.237632
38. Xu J-H, Zhang B-X, Yan H-Z, et al. (2024) Sliding mode—Extended state observer control strategy to improve energy transfer of PEMFC connected DC-DC boost converter system. *Sustainable Energy Technol Assess* 63: 103654. https://doi.org/10.1016/j.seta.2024.103654

39. Lee H, Utkin VI (2007) Chattering suppression methods in sliding mode control systems. *Annu Rev Control* 31: 179–188. https://doi.org/10.1016/j.arcontrol.2007.08.001
40. Swikir A, Utkin V (2016) Chattering analysis of conventional and super twisting sliding mode control algorithm. *2016 14th International Workshop on Variable Structure Systems (VSS)*, 98–102. https://doi.org/10.1109/VSS.2016.7506898
41. Castillo I, Freidovich LB (2020) Describing-function-based analysis to tune parameters of chattering reducing approximations of Sliding Mode controllers. *Control Eng Pract* 95: 104230. https://doi.org/10.1016/j.conengprac.2019.104230
42. Kuchwa-Dube C, Pedro JO (2022) Chattering performance criteria for multi-objective optimisation gain tuning of sliding mode controllers. *Control Eng Pract* 127: 105284. https://doi.org/10.1016/j.conengprac.2022.105284
43. Ali K, Ullah S, Mehmood A, et al. (2022) Adaptive FIT-SMC approach for an anthropomorphic manipulator with robust exact differentiator and neural network-based friction compensation. *IEEE Access* 10: 3378–3389. https://doi.org/10.1109/ACCESS.2021.3139041
44. Pedro JO, Dangor M, Dahunsi OA, et al. (2018) Dynamic neural network-based feedback linearization control of full-car suspensions using PSO. *Appl Soft Comput* 70: 723–736. https://doi.org/10.1016/j.asoc.2018.06.002
45. Mac TT, Copot C, Duc TT, et al. (2016) AR.Drone UAV control parameters tuning based on particle swarm optimization algorithm. *2016 IEEE International Conference on Automation, Quality and Testing, Robotics (AQTR)*, 1–6. https://doi.org/10.1109/AQTR.2016.7501380
46. Laware AR, Talange DB, Bandal VS (2018) Evolutionary optimization of sliding mode controller for level control system. *ISA Trans* 83: 199–213. https://doi.org/10.1016/j.isatra.2018.08.011
47. Rodríguez-Molina A, Mezura-Montes E, Villarreal-Cervantes MG, et al. (2020) Multi-objective meta-heuristic optimization in intelligent control: A survey on the controller tuning problem. *Appl Soft Comput* 93: 106342. https://doi.org/10.1016/j.asoc.2020.106342
48. Deb K, Agrawal S, Pratap A, et al. (2000) A fast elitist non-dominated sorting genetic algorithm for multi-objective optimization: NSGA-II. In: Schoenauer M, Deb K, Rudolph G, et al. (Eds), *Parallel Problem Solving from Nature PPSN VI*, Berlin, Heidelberg, Springer, 849–858. https://doi.org/10.1007/3-540-45356-3_83
49. Mezura-Montes E, Reyes-Sierra M, Coello CA (2008) Multi-objective optimization using differential evolution: A survey of the state-of-the-art. *Stud Comput Intell* 143: 173–196. https://doi.org/10.1007/978-3-540-68830-3_7
50. Coello Coello CA, Lechuga MS (2002) MOPSO: A proposal for multiple objective particle swarm optimization. *Proceedings of the 2002 Congress on Evolutionary Computation. CEC'02 (Cat. No.02TH8600)* 2: 1051–1056. https://doi.org/10.1109/CEC.2002.1004388
51. Yan Y, Du H, Wang Y, et al. (2022) Multi-Objective asymmetric sliding mode control of connected autonomous vehicles. *IEEE Trans Intell Transp Syst* 23: 16342–16357. https://doi.org/10.1109/TITS.2022.3149985
52. Rezapour J, Sharifi M, Nariman-zadeh N (2011) Application of fuzzy sliding mode control to robotic manipulator using multi-objective genetic algorithm. *2011 International Symposium on Innovations in Intelligent Systems and Applications*, 455–459. https://doi.org/10.1109/INISTA.2011.5946144

53. Acharya DS, Gude S (2021) A multi-objective integral sliding mode controller for magnetic levitation plant. In: Reddy MJB, Mohanta DKr, Kumar D, et al. (Eds), *Advances in Smart Grid Automation and Industry 4.0*, Singapore, Springer, 177–185. https://doi.org/10.1007/978-981-15-7675-1_17
54. Zarchan P, Musoff H (2015) Extended Kalman Filtering. *Fundamentals of Kalman Filtering: A Practical Approach, Fourth Edition*, American Institute of Aeronautics and Astronautics, Inc., 225–259. https://doi.org/10.2514/5.9781624102776.0225.0260
55. Suresh K, Parimalasundar E, Arunraja A, et al. (2025) High-efficiency stepdown/step-up converter for series-connected energy storage system. *Sci Rep* 15: 7726. https://doi.org/10.1038/s41598-025-92234-y
56. Kolli A, Gaillard A, De Bernardinis A, et al. (2015) A review on DC/DC converter architectures for power fuel cell applications. *Energy Convers Manage* 105: 716–730. https://doi.org/10.1016/j.enconman.2015.07.060
57. Lü X, Qu Y, Wang Y, et al. (2018) A comprehensive review on hybrid power system for PEMFC-HEV: Issues and strategies. *Energy Convers Manage* 171: 1273–1291. https://doi.org/10.1016/j.enconman.2018.06.065
58. Erickson RW, Maksimović D (2001) Converter Circuits. In: Erickson RW, Maksimović D (Eds), *Fundamentals of Power Electronics*, Boston, MA, Springer US, 131–184. https://doi.org/10.1007/0-306-48048-4_6
59. Vijayaraghavan K, DeVaal J, Narimani M (2015) Dynamic model of oxygen starved proton exchange membrane fuel-cell using hybrid analytical-numerical method. *J Power Sources* 285: 291–302. https://doi.org/10.1016/j.jpowsour.2015.03.103
60. Beigi A, Romey W, Vijayaraghavan K (2024) Extended Kalman filter for quantifying hydrogen leaks in PEM fuel cells by estimating oxygen concentration. *Int J Hydrogen Energy* 78: 907–917. https://doi.org/10.1016/j.ijhydene.2024.06.094
61. Amphlett JC, Baumert RM, Mann RF, et al. (1995) Performance modeling of the ballard mark IV solid polymer electrolyte fuel cell: I. mechanistic model development. *J Electrochem Soc* 142. https://doi.org/10.1149/1.2043866
62. Wang C, Nehrir MH, Shaw SR (2005) Dynamic models and model validation for PEM fuel cells using electrical circuits. *IEEE Trans Energy Convers* 20: 442–451. https://doi.org/10.1109/TEC.2004.842357
63. Larminie J, Dicks A (2003) Fuel cell systems analysed. *Fuel Cell Systems Explained*, John Wiley & Sons, Ltd, 369–389. https://doi.org/10.1002/9781118878330.ch11
64. Haddad WM, Chellaboina V (2008) Nonlinear dynamical systems and control. *A Lyapunov-Based Approach, Princeton University Press*. https://doi.org/10.1515/9781400841042
65. Mobayen S (2015) An adaptive chattering-free PID sliding mode control based on dynamic sliding manifolds for a class of uncertain nonlinear systems. *Nonlinear Dyn* 82: 53–60. https://doi.org/10.1007/s11071-015-2137-7
66. Eker İ (2006) Sliding mode control with PID sliding surface and experimental application to an electromechanical plant. *ISA Trans* 45: 109–118. https://doi.org/10.1016/S0019-0578(07)60070-6
67. Mobayen S, Karami H, Fekih A (2021) Adaptive nonsingular integral-type second order terminal sliding mode tracking controller for uncertain nonlinear systems. *Int J Control Autom Syst* 19: 1539–1549. https://doi.org/10.1007/s12555-020-0255-6

68. Mobayen S, Tchier F (2017) A novel robust adaptive second-order sliding mode tracking control technique for uncertain dynamical systems with matched and unmatched disturbances. *Int J Control Autom Syst* 15: 1097–1106. https://doi.org/10.1007/s12555-015-0477-1
69. Utkin V (1977) Variable structure systems with sliding modes. *IEEE Trans Autom Control* 22: 212–222. https://doi.org/10.1109/TAC.1977.1101446
70. Zhu WQ, Huang ZL, Ko JM, et al. (2004) Optimal feedback control of strongly non-linear systems excited by bounded noise. *J Sound Vib* 274: 701–724. https://doi.org/10.1016/S0022-460X(03)00746-6
71. Napole C, Barambones O, Derbeli M, et al. (2021) Advanced trajectory control for piezoelectric actuators based on robust control combined with artificial neural networks. *Appl Sci* 11: 7390. https://doi.org/10.3390/app11167390
72. Panda S, Sahu BK, Mohanty PK (2012) Design and performance analysis of PID controller for an automatic voltage regulator system using simplified particle swarm optimization. *J Franklin Inst* 349: 2609–2625. https://doi.org/10.1016/j.jfranklin.2012.06.008
73. Chang W-D, Chen C-Y (2014) PID controller design for MIMO processes using improved particle swarm optimization. *Circuits Syst Signal Process* 33: 1473–1490. https://doi.org/10.1007/s00034-013-9710-4
74. Miettinen K (1999) Nonlinear multiobjective optimization. Boston, MA, Kluwer Academic Publishers. https://doi.org/10.1007/978-1-4615-5563-6
75. US EPA (2015) EPA Urban Dynamometer Driving Schedule (UDDS). Available from: https://www.epa.gov/emission-standards-reference-guide/epa-urban-dynamometer-driving-schedule-udds.

AIMS Press